emerald PUBLISHING

Rapid Prototyping J

Development of dual nozzle slurry extrusion 3D printer by integrating material extrusion and photopolymerization for the fabrication of engineered ceramics

Journal:	*Rapid Prototyping Journal*
Manuscript ID	RPJ-09-2024-0387.R1
Manuscript Type:	Original Article
Keywords:	Engineered ceramics, Additive Manufacturing, Zirconia slurry, material extrusion process, VAT photopolymerization process

SCHOLARONE™
Manuscripts

Development of dual nozzle slurry extrusion 3D printer by integrating material extrusion and photopolymerization for the fabrication of engineered ceramics

Abstract

Purpose

This research focuses on developing a dual-nozzle slurry-based extrusion 3D printer capable of fabricating intricate zirconia structures. The designed 3D printer combines material extrusion and photopolymerization technologies to improve material diversity, precision, and cost-effectiveness.

Design/methodology/approach

The 3D printer design incorporates ultraviolet curing to instantly cure extruded zirconia slurry thereby, eliminating the need for a step-wise curing procedure. Printing parameters were optimized to achieve high-quality prints, and supports made of polyethylene terephthalate glycol (PETG) were used for intricate geometries. The printability and mechanical properties were evaluated for two different zirconia slurry compositions: 70/30 and 80/20 powder-to-resin weight percentages. The printed green body was subjected to a two-phase sintering process.

Findings

The 3D printer fabricated structures with features subtending angles greater than 50 degrees and a filling density above 80% without any supports. Shrinkage analysis showed the 80/20 composition resulted in higher density parts, with shrinkage ratios of 25.23%, 26.23%, and 27.26% along the X, Y, and Z axes, respectively. The sintered objects displayed hardness (1525 HV) and flexural strength (117 MPa), with minimal porosity.

Originality/value

This study demonstrates the development of a cost-effective dual-nozzle 3D printer that can effectively fabricate functional parts with complex material compositions and geometries that can cater to the futuristic requirements of high-end industries.

Keywords: *Engineered ceramics; additive manufacturing; zirconia slurry; material extrusion process; VAT photopolymerization process*

Abbreviations:

ATZ: Alumina toughened zirconia

ZTA: Zirconia toughened alumina

CLS: Ceramic laser sintering

AM: Additive manufacturing

FDM: Fused deposition modeling

VPP: VAT photopolymerization

SLA: Stereolithography

DLP: Digital light processing

PETG: Polyethylene terephthalate glycol

UV: Ultraviolet

TMPTA: Trimethylolpropane triacrylate

HDDA: Hexanediol diacrylate

TPO: trimethyl benzoyl phosphine oxide

LED: Light-emitting diode

SEM: Scanning electron microscopy

HV: Vicker's hardness

1. Introduction

Additive manufacturing of engineered ceramics has emerged as one of the most sought topics in recent years due to its flexibility, speed, and cost of fabrication (Lakhdar, Tuck et al. 2021, Pelz, Ku et al. 2021, Cova, Hostaša et al. 2023) Engineered ceramics, especially oxides such as alumina and zirconia are in high demand due to their high melting point, excellent strength, and biocompatibility(Petit, Montanaro et al. 2018). Moreover, recent advancements have paved the way for the fabrication of a special class of engineered ceramics known as 'technical ceramics' (Piconi, Condo et al. 2014). Alumina-toughened zirconia (ATZ) and zirconia-toughened alumina (ZTA) are the two most common technical ceramics that are extensively used in several electronic, biomedical, and refractory industries (Olhero, Mesquita-Guimarães et al. 2022). Traditionally, these ceramics are fabricated either using powder compaction and sintering or hot isostatic pressing. Though these techniques successfully fabricated engineered ceramics with negligible porosity, the control over the fabrication process is constrained. Fabrication of intricate geometries that can deliver high mass-specific performances is often dealt with by extensive secondary/post-processing. These secondary post-processing steps significantly increased the cost of the product (~70% of the total manufacturing expenses) (Olhero, Mesquita-Guimarães et al. 2022).

In recent years of progress in the additive manufacturing field, several innovative technologies have emerged for the fabrication of engineered ceramic components (Lakhdar, Tuck et al. 2021). With better control over the fabrication process, intricately shaped engineered ceramics can be 3D printed for lightweight high-performance applications. Furthermore, additive manufacturing also reduces the secondary post-processing, thereby significantly reducing material wastage (Jiang, Xu et al. 2019, Nyika, Mwema et al. 2022). Several additive manufacturing technologies have emerged over the past decade for the fabrication of engineered ceramics. Tang et al. designed the ceramic laser sintering (CLS) process for the fabrication of silica powder and silica sol suspended in water. The study also developed the slurry coating system which would pave the slurry over the thin layer which was subsequently sintered using a laser source (Yen and Tang 2008). The CLS process is further modified to fabricate high-strength alumina parts using polymer-coated ceramic slurry (Tang, Chiu et al. 2011). Though this technology proved to be a

milestone in the additive manufacturing of engineered ceramics, it had several shortcomings. The process utilized excessive polymeric binder due to which, de-binding was not complete. Furthermore, the strength of the fabricated component was not satisfactory(Tang, Chiu et al. 2011). Apart from the CLS process, two basic slurry-based AM techniques that can deliver low-cost ceramic components are vat photopolymerization and material extrusion (Lakhdar, Tuck et al. 2021).

Material extrusion, commonly known as Fused Deposition Modeling (FDM), is a widely used technique that involves the deposition of melted thermoplastic materials layer by layer to build a 3D object (Wang, Wang et al. 2024). While FDM is cost-effective and easy to use, it is generally restricted to thermoplastic material applications. Several researches have been carried out to inculcate a slurry extrusion setup in the traditional extrusion printer that can extrude a controlled amount of slurry onto the print bed (Huang, Mason et al. 2006, Lewis 2006, Nadkarni and Smay 2006, Romario, Bhat et al. 2024). Such technologies are broadly classified into water-based extrusion and wax-based extrusion processes (Lakhdar, Tuck et al. 2021). Though ceramic extrusion technologies offer considerably a low-cost printing process, it has several associated disadvantages. Shape retention of the extruded slurry is the major issue due to the semi-viscous nature of the slurry (Hu, Mikolajczyk et al. 2021). In order to ensure shape retention, the viscosity of the slurry has to be increased which increases the risk of nozzle clogging and damage (Tang, Yang et al. 2019). To obtain accurate print quality, care has to be taken to ensure complete curing of the first layer before printing the successive layers. This would exponentially increase the printing time which makes it highly infeasible.

On the other hand, VAT photopolymerization (VPP), utilized in technologies such as Stereolithography (SLA) and Digital Light Processing (DLP), involves curing liquid resins using a UV light source to form solid structures (Jankowska, Chachaj-Brekiesz et al. 2023). This method offers high resolution, and surface finish, and can fabricate near net-shaped structures. However, this technology is feasible with a limited number of materials. Furthermore, this process involves a cleaning stage after the fabrication of each layer to prevent contamination. This step increases the time as the print bed has to raise and rotate towards the cleaning vat after the printing of each layer (Jiang, Romario et al. 2023, Romario, Bhat et al. 2024)

This study combines these two processes to overcome the limitations posed by the two technologies. By combining these two processes, the proposed multi-material 3D printer aims to

leverage the strengths of both techniques to enhance material diversity and precision while enabling low-cost fabrication. However, the integration of material extrusion and photopolymerization presents several technical challenges, including synchronizing the two printing processes, developing compatible materials, and optimizing print parameters to ensure cohesive bonding between different materials. This study addresses these challenges through innovative design and engineering solutions. The printer's architecture is meticulously designed to facilitate seamless switching between extrusion and photopolymerization, enabling the creation of complex geometries with varied material properties. This paper details the design, implementation, and testing phases of the multi-material 3D printer. It includes an in-depth analysis of the printer's systems, developing specialized material compatible with both extrusion and photopolymerization, and evaluating printed objects' mechanical properties and accuracy. Through rigorous testing and validation, the proposed multi-material 3D printer demonstrates its capability to produce high-quality, functional parts with complex material compositions. Moreover, technology allows for direct fabrication without the requirement of post-processing and thus, the resulting products can be customized to meet specific needs.

2. Material and Methods

The three-dimensional printer developed in this study uses dual nozzles to extrude photocurable slurry (zirconia) and polyethylene terephthalate glycol (PETG). The PETG acts as a support material that can withhold the semi-viscous slurry at critical locations. The design of slurry extrusion is based on the concept of a photopolymer extrusion three-dimensional printer. To solidify, the extruded slurry is exposed to a suitable wavelength of UV light. This section will explain the material preparation, machine design, and processing parameters of the developed 3D printer and explain detailed experimental procedures.

2.1 Material Preparation

The zirconia slurry used in this study is prepared by mixing resin, photoinitiator, zirconia powder, and dispersant. Different combinations were prepared and experimented with to find a suitable proportion of powder and resin. Figure 1 schematically represents the stepwise procedures involved in preparing zirconia slurry.

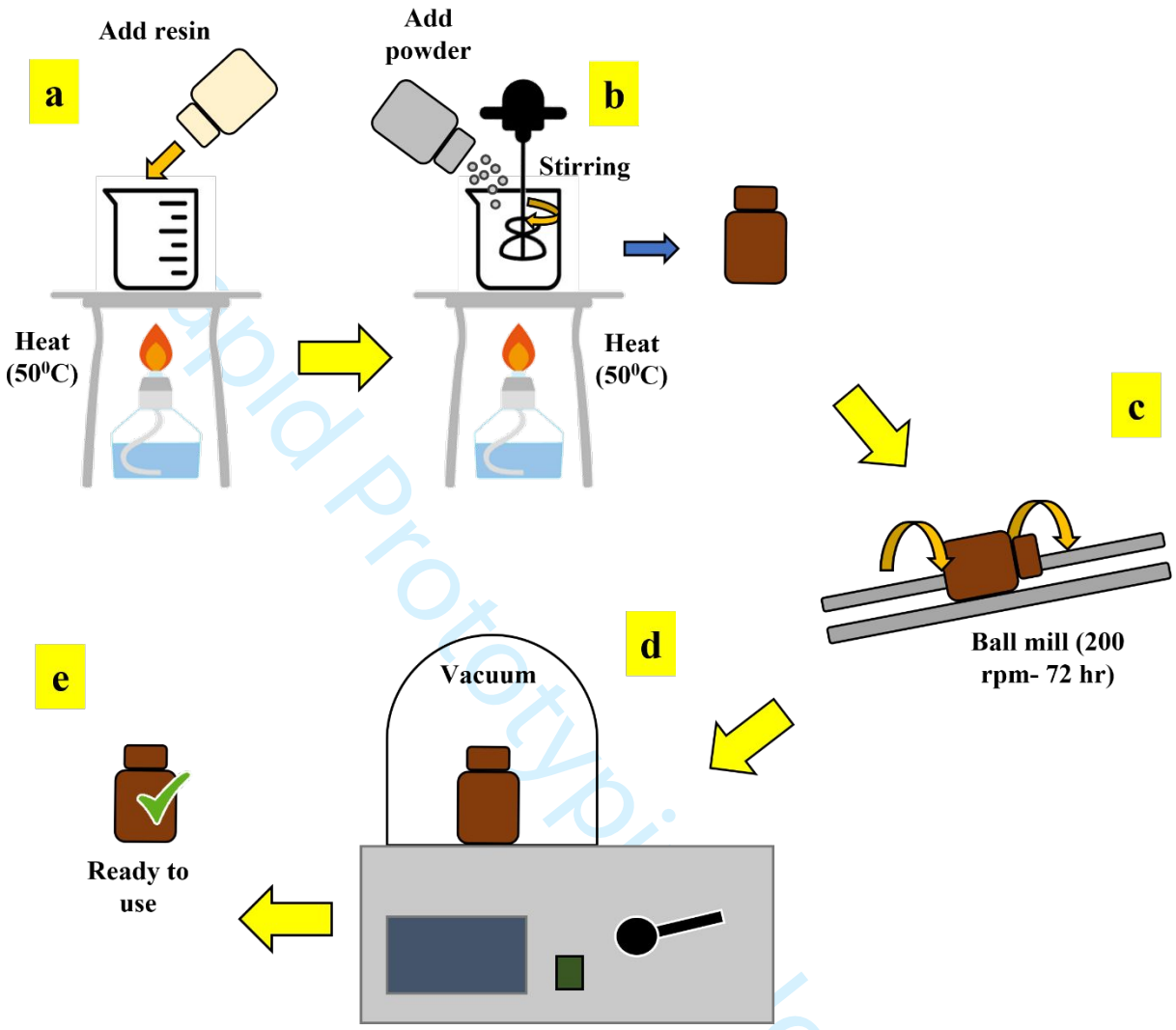

Figure 1: Slurry preparation process (a) Resin heating (b) Slurry mixing (c) Ball milling (d) Vacuum process (e) Slurry ready to use.

The process of making the zirconia slurry involves several detailed steps. First, the resin is heated to 50°C to facilitate thorough mixing with the photoinitiator (Figure 1a). While maintaining a constant temperature, additives are added to the resin-photoinitiator mixture as shown in Figure 1b. The mixture is constantly stirred during the addition process to ensure a homogenous distribution of additives without any lumps. Once mixing is complete, the slurry mixture is poured into a bottle, sealed, and placed in a roller and ball milled for 72 hours at 200 rpm (Figure 1c). This

step is necessary to further ensure homogenization of the mixture without any lumps. After ball milling, bottles undergo a vacuum process as shown in Figure 1d at a negative pressure of 1.5 Torr to eliminate air bubbles from the slurry. Once the trapped air bubbles are eliminated, the slurry is ready to be used (Figure 1e).

The zirconia powder used in this study is typically known as 'ZT3Y-010OA', procured from Zipro Tech., Taiwan). The specialized yttrium stabilized zirconia powder contains 3 mol % of yttrium oxide. Yttria is added to change the phase transformation temperature range of zirconium dioxide, making it stable cubic and tetragonal crystals at room temperature. The detailed composition of zirconia used in this study is listed in Table 1. The mean particle diameter of zirconium dioxide powder is approximately 0.5 µm, however, fine particles are sensitive to moisture and tend to form agglomerates. Before preparing the slurry, it is essential to sieve the zirconia powder and remove any excessively big particles.

Table 1: The detailed specifications of zirconia powder used in this study (ZT3Y-010OA).

Characteristic	**Unit**	**ZT3Y-010OA**	**Remarks**
$Zr(Hf)O_2$	(wt%)	94.5	
Y_2O_3	(wt%)	5.64	
SiO_2	(wt%)	0.0016	
Fe_2O_3	(wt%)	0.0004	
Na_2O	(wt%)	ND	
CaO	(wt%)	ND	
Moisture	(wt%)	0.23	150^0C/5min
Ignition Loss	(wt%)	0.33	1100^0C/1h
Sintered Density	(g/cm^3)	6.05	1550^0C/3h
Particle Size – D_{10}	(µm)	0.14	
Particle Size – D_{50}	(µm)	0.21	
Particle Size – D_{90}	(µm)	0.51	

Table 2: TMPTA and HDDA specifications along with their structural formation and

characteristics.

Resin	**HDDA**	**TMPTA**
Structure	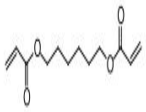	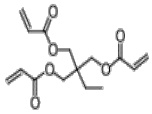
Molecular weight(g/mol)	226	296
Density (g/cm^3)	1.01	1.09-1.12
Viscosity (cps)	5-10	70-120
Characteristic	low viscosity, high adhesion, good reactivity	medium viscosity, fast curing, high hardness

In this study, two different resins: TMPTA and HDDA resins purchased from Guojing Chemical Co., Ltd., Taiwan. Table 2 outlines the detailed specifications of these two resins along with their structural formation and characteristics. The photoinitiator TPO was added to the resin to synthesize a photosensitive resin that solidifies under 405 nm wavelength. Table 3. Illustrates the composition of the zirconia slurry used in this study. Two different compositions are used with the solid loading (i.e. zirconia powder) of 70% and 80%.

Table 3: Composition of zirconia slurry.

Composition	**Zirconia**		**HDDA**		**TMPTA**		**TPO**	
	(wt.%)	(vol.%)	(wt.%)	(vol.%)	(wt.%)	(vol.%)	(wt.%)	(vol.%)
70/30	70.00	30.56	9.25	22.71	19.25	43.40	1.5	3.32
80/20	80.00	40.55	18.50	54.29	0	0	1.5	3.86

2.2 Development of Dual-Nozzle Slurry Extrusion 3D Printer

The dual-nozzle slurry extrusion 3D printer is constructed using 30 x 30 mm aluminum frames which provides the printer with excellent stability and robustness. With overall dimensions

of 740 x 700 x 570 mm, the printer operates on a cartesian coordinate system which is known for its simplicity, stability, and suitability for high-speed and high-precision 3D printing. The working range of the machine is 240 x 180 x 145 mm, providing ample space for various printing tasks. The construction of the 3D printer is shown in Figure 2a. As can be observed in Figure 2a, the printer is equipped with two nozzles, each specialized for the extrusion of different materials. The material feeder system delivers the zirconia slurry to the slurry printing nozzle. Equipped with a heat bed capable of heating up to 80 degrees Celsius, the machine ensures optimal adhesion of materials to the bed. For PETG printing, it uses a 0.4 mm diameter nozzle, which is heated to 240 degrees Celsius to facilitate effective extrusion.

Figure 2b shows the construction of the material feeder system. It consists of a material tube where the prepared zirconia slurry is stored. The material tube is equipped with a barrel extrusion and tube slider which eventually pushes the zirconia slurry upon feeder motor rotation. The amount of slurry extrusion depends on the rotation of the feeder motor which can be controlled as per the requirement. This mechanism offers better control and stability compared to the peristaltic pumps.

Figure 2c shows the slurry extrusion nozzle design. The extrusion head is equipped with 405 nm UV lights on both sides to maximize the energy directed at the extruded slurry. The energy output is precisely focused on the extruded slurry for optimal curing. This meticulous design and advanced features make the machine highly efficient for producing accurate and detailed multi-material parts. Furthermore, the nozzle at the end of the extrusion mechanism can be easily replaced according to specific product requirements.

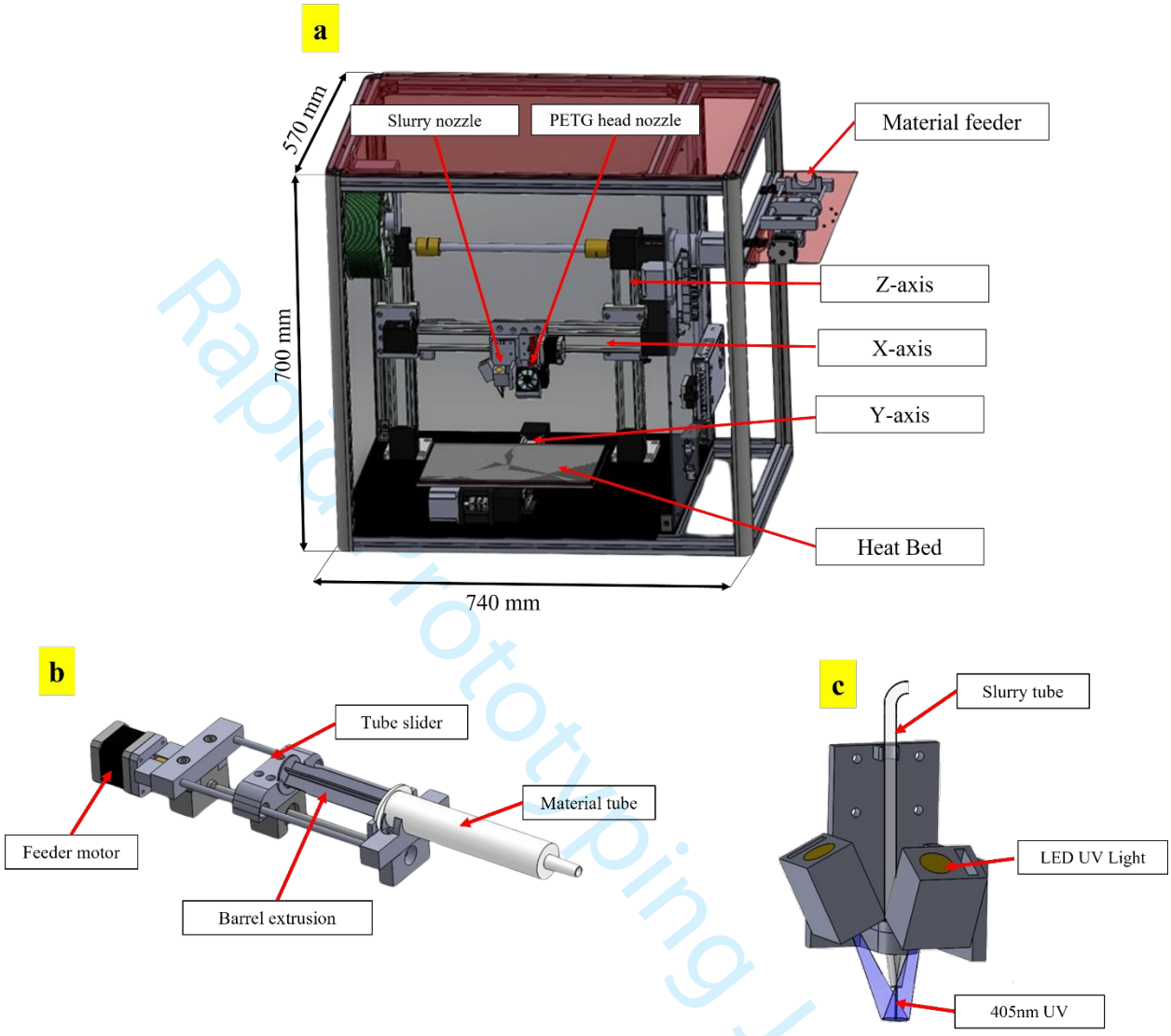

Figure 2: The development of dual-nozzle slurry extrusion 3D printer: (a) overall 3D design of slurry printing, (b) Construction of the material feeder system, and (c) slurry extrusion nozzle.

For zirconia slurry, the extrusion mechanism is designed with a tube system that can be pressed, offering enhanced accuracy and control compared to peristaltic pumps, thanks to the barrel pusher's controllability. with the LED output focused precisely on the.

2.3 Evaluation of Optimal Printing Parameters

After ensuring the working of the 3D printer, it is essential to ascertain the suitable printing

parameters. These parameters are crucial for ensuring the stability of machine operation and the production of printed parts with adequate mechanical properties. Adjusting these parameters will enhance the efficiency and reliability of the printing procedure, leading to top-notch results that adhere to the specified criteria.

Printing parameters that significantly influence extrusion 3D printing include nozzle diameter, printing speed, and layer thickness (Shao, Zhao et al. 2017, Koski, Onuike et al. 2018, Li, Ghazanfari et al. 2018, Tang, Yang et al. 2019, Qian, Yang et al. 2020, Yu, Zhang et al. 2020, Zhang, Lin et al. 2020). In this study, these parameters were used as variables for evaluating the printing efficacy of the developed 3D printer. The nozzle diameter and layer thickness directly affect the accuracy of extrusion printing: the smaller the nozzle diameter and layer thickness, the higher the printing accuracy, but it takes a longer time to print. Based on the previous research shows in Table 3, the nozzle diameter ranges from 0.2 mm to 0.8 mm. Various nozzle diameters are tested in this study to determine the optimal size for smoothly dispensing ceramic slurry. Based on reference literature, the layer thickness ranges from 0.1 mm to 0.6 mm. Given that the machine used in this research is based on a material extrusion process, the layer thickness is set to 0.2 mm.

Table 4: Integration of printing parameters for extrusion slurry 3D printers.

Authors	**Material Composition**	**Nozzle Diameter**	**Printing Speed**	**Layer Thickness**
Wenbin Li et al. (Li, Ghazanfari et al. 2018)	ZrO_2 50 Vol% + Distilled Water	0.2 0.6		0.08 0.4
Tianyu Yu et al. (Yu, Zhang et al. 2020)	ZrO_2 60 Vol% + Hydrogel	1	60	0.6
Lei Qian et al. (Qian, Yang et al. 2020)	ZrO_2 84 Vol% + Hydrogel	0.41	20	0.4
Hui Ping Shao et al. (Shao, Zhao et al. 2017)	ZrO_2 50 Vol% + Hydrogel	0.5	20	0.4

Zhinan Zhang et al. (Zhang, Lin et al. 2020)	ZrO_2 47.65 Vol% + Hydrogel	0.41	12.45	0.32 0.36 0.41
Caitlin Koski et al. (Koski, Onuike et al. 2018)	Calcium phosphate + Corn Starch + water	0.7 0.9	40 70	1.5
Shiyan Tang et al. (Tang, Yang et al. 2019)	Al_2O_3 50 Vol% + Hydrogel	0.4 0.5 0.6	10 15 20	60% 70% 80% Of nozzle diameter

The printing speed is influenced by the viscosity of the ceramic slurry. Lower viscosity ensures smooth extrusion but increases printing time and loses integrity (i.e. shape retention). According to the previous research (Asif, Lee et al. 2018), the best printing results are achieved when the extrusion slurry viscosity is between the range of 15,000 cp and 18,000 cp. When the slurry flows through a tube, its viscosity is affected by shear force (Romario, Bhat et al. 2024). Through viscosity testing, the relationship between viscosity and shear rate can be established, which is inversely proportional (Sangroniz Agudo, Fernández San Martín et al. 2023). The speed of the fluid flow is proportional to the shear rate; thus, a faster printing speed results in lower viscosity. The relationship between printing speed (v) and shear rate ($\dot{y}$) is described by Equation 1:

$$\dot{y} = \frac{8v}{\mathrm{d}} \quad (1)$$

where ‘d’ is the diameter of the nozzle. After determining the nozzle diameter, the corresponding shear rate for a viscosity of 15,000 cp to 18,000 cp can be found based on the relationship between viscosity and shear rate. The printing speed can then be calculated using Equation 1.

This study utilizes PETG as support for the printed parts. Using a moderate amount of support

can help fabricate the intricate shapes effectively. However, the surfaces in contact with the support would appear rough due to the texture of the PETG layers. Thus, minimizing the support requirements is important to increase the printed parts' surface quality. It is necessary to test at which angles the printing process can perform optimally with support requirements. This research uses a pyramid benchmark to evaluate the printing tests (Figure 3). The base of the pyramid is a triangle with sides measuring 15 x 15 mm. The height is adjusted to change the angle θ.

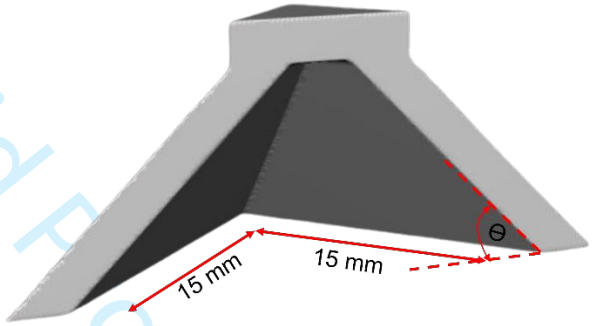

Figure 3: Pyramid benchmark printing to evaluate the optimal angle that can be printed without the use of PETG support material.

2.4 Viscosity

In this study, a viscosity test was conducted to determine the optimal viscosity required for smooth slurry flow during the printing process. To achieve this, the slurry was prepared to attain the appropriate viscosity, ensuring a high level of printability for the model. A viscometer (Brookfield DV3T, Ametek, Massachusetts, United Kingdom) was utilized to measure the slurry's viscosity coefficient.

2.5 Thermal Analysis

Once the green bodies are printed, thermogravimetric analysis (TGA) is employed to analyze changes in the properties of ceramic slurries and support materials with increasing temperature. To avoid extreme volume changes in the resin and support material during the debinding process, the sintering temperature must be carefully regulated. The excessive volumetric changes may affect the dimensional and structural integrity of the printed part. Differential scanning calorimetry (DSC) measurements were conducted using a Hitachi STA200 thermal analysis instrument. Samples weighing 10 mg were prepared for this analysis and placed in titanium crucibles. Pure

nitrogen was used as the purge gas, with a flow rate of 100 mL/min. During all DSC measurements, each sample was heated at a rate of 10°C/min until it reached a temperature of 900°C.

The two-phase sintering process is employed in this study to obtain the final product. In the first stage, the photopolymerization resin in the printed green body undergoes a debinding process, causing initial volume shrinkage. In the second stage, the green body is heated to produce crystals which would further shrink the green body. In this study, the green body was printed with the dimension of 10 x 10 x 10 mm. After the sintering process, the dimension of the final product is compared with the green body to evaluate the volume of shrinkage. These shrinkage results can be used to adjust size allowances during the 3D design process.

2.6 Energy Dispersive Spectroscopy (EDS) Analysis

Energy Dispersive X-ray Spectroscopy (EDS) was performed using a TM4000Plus microscope (Hitachi, Japan). This technique was utilized to analyze the chemical composition of the material, providing elemental mapping and quantitative data. The results were cross-referenced to ensure consistency with the expected material composition and to identify any impurities or deviations.

2.7 X-Ray Diffraction (XRD) Analysis

X-Ray Diffraction (XRD) was conducted using an Empyrean diffractometer (Malvern Panalytical, United Kingdom). This technique was employed to determine the crystalline structure and phase composition of the material. The diffraction patterns were obtained by scanning over a range of 2θ angles, and the results were analyzed to identify and quantify the phases present.

2.8 Evaluation of Mechanical Properties

To ensure the fabricated part has sufficient strength, the mechanical properties of the printed ceramic parts after sintering were measured. The hardness tests and three-point bending tests were carried out as per the Advanced Ceramics Vickers specifications from ASTM (American Society for Testing & Materials). The Vickers hardness of zirconia ceramic molds was measured as per the ASTM C1327-03 standards. The hardness value of each sample is evaluated using Equation 2. The technique involves using a diamond indenter in the form of a regular square pyramid with a face angle of 136°, which presses onto the surface of the material being tested with a specific load

(F). After maintaining the pressure for 15 seconds, an optical microscope is used to observe and measure the square indentation on the surface of the material. The diagonal lengths of the indentation are measured, and the arithmetic mean of the two perpendicular diagonal lengths (l_1 and l_2) is calculated to obtain the average diagonal length (d). The term (g) in Equation 2 is the acceleration due to gravity. The Vickers hardness value is then calculated using the formula:

$$\mathrm{HV} = \frac{2F \times \sin\left(\frac{136^\circ}{2}\right)}{g \times d^2} \quad (2)$$

Depending on the sintering conditions and the material's structure, different hardness values may be obtained at different locations on the same object. Therefore, hardness testing was conducted at various points following ASTM standards.

Apart from the hardness evaluation, the three-point bending tests were conducted to evaluate the flexural strength of the printed ceramic specimens. The dimension of the specimens for this study was: 25 mm x 3.5 mm x 2 mm, which is in accordance with ASTM C1161-13 standards. The clamp distance used in this study was set to 20 mm, and the diameter of the round head was 3 mm. During the test, the speed of the test rod was maintained constantly at 0.2 mm/min until the test rod broke. The maximum load experienced during testing was recorded. The flexural strength is calculated as per the Equation 3.

$$S = \frac{3PL}{2bh^2} \quad (3)$$

where ‘P’ is the maximum failure load, ‘L’ is the span of the test bar, ‘b’ is the width of the test bar, and ‘h’ is the height of the test bar.

2.9 SEM Analysis

A field emission scanning electron microscope (SEM, Hitachi SU-70) operating at an accelerating voltage of 5 kV was used to observe the composite morphology transformation of the sintered objects. SEM images were also used to identify grain size and axis contained in the sintered objects.

3. Results and Discussion

3.1 Printing Parameters Assessment

After ensuring that the 3D printer works efficiently, the printing parameters are optimized for the best possible results in terms of print quality and speed of printing. The printing parameters that significantly influence 3D extrusion printing include nozzle diameter, printing speed, and layer thickness.

3.1.1 Nozzle diameter selection

This study aims to examine the appropriate nozzle diameter that can be used for ceramic slurry printing without compromising the quality of print. The nozzle diameter for extrusion printing ranges from approximately 0.2 mm to 0.8 mm. At a diameter of 0.2 mm, printing failed due to clogging of slurry in the nozzle channel. Printing could be completed with a 0.4 mm nozzle, although occasional blockage occurred. These blockages were likely caused by particles in the ceramic slurry that were not fully dispersed, leading to nozzle clogs. The experimental results obtained with a 0.6 mm nozzle were convincing without any clogging. Thus, a 0.6 mm diameter nozzle is used for printing, as it strikes a balance between preventing clogs and maintaining the quality of the print. A 0.8 mm diameter nozzle also prints well without any particle clogging. However, the surface finish and accuracy of the final product are compromised due to the large diameter of the nozzle. If higher accuracy is required, a 0.4 mm nozzle can also complete the printing, but there is a risk of material clogging.

3.1.2 Viscosity

The viscosity of the slurry significantly influences the success of the printing process. The selection of slurry compositions (Table 3), plays a critical role in determining the printability and quality of the printed parts. An optimal viscosity ensures smooth purging during the process and results in printed models with high-density material properties.

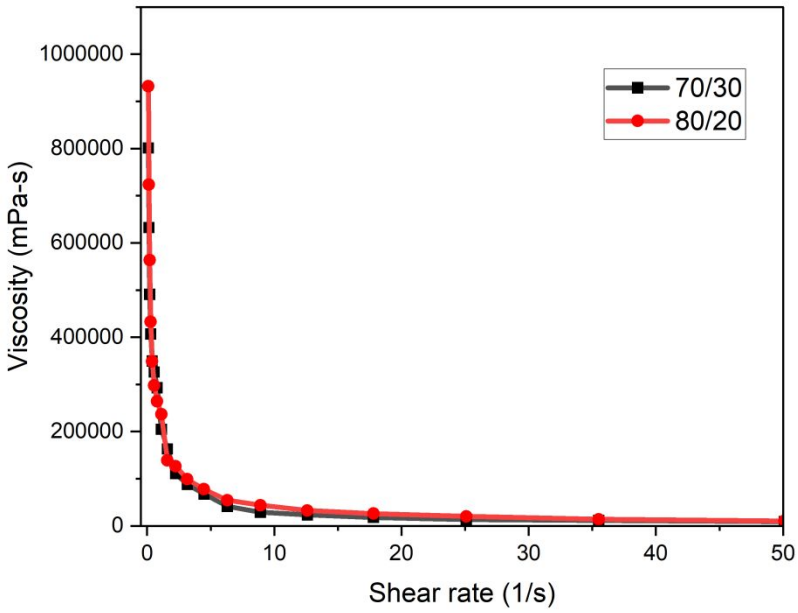

Figure 4. Viscosity ratio results of various slurry compositions. (70/30, 80/20).

Figure 4 illustrates the relationship between shear rate and viscosity for the resin compositions of 70/30 and 80/20. The data demonstrate a typical shear-thinning behavior, where the viscosity decreases as the shear rate increases. The 80/20 resin composition exhibits slightly higher viscosity across the shear rate range compared to the 70/30 composition. This is expected, as the higher solid content in the 80/20 ratio contributes to increased internal resistance and viscosity. However, the difference in viscosity between the two compositions becomes less pronounced at higher shear rates, indicating a similar flow behavior under applied shear stress. Optimizing the resin composition is crucial for striking a balance between mechanical performance and printability.

3.1.3 Printing speed

The printing speed is influenced by the viscosity coefficient of the ceramic slurry. This study evaluates the printing speed for two different compositions (i.e. zirconia/resin = 70/30 and 80/20) as detailed in Table 3. The viscosity analysis is carried out to understand the shear rate characteristics for these two compositions. Using Equation (1), the appropriate printing speed for

viscosities ranging from 15000 cp to 18000 cp was calculated. The printing speeds for each composition at different viscosities are shown in Table 5.

Table 5: Printing speed and corresponding shear rate for zirconia slurry (70/30 and 80/20).

70/30 (70% zirconia and 30% resin)				
Viscosity (cp)	15000	16000	17000	18000
Corresponding shear rate	36.76	34.70	32.63	30.56
Printing speed (mm/s)	7.35	6.94	6.53	6.11
80/20 (80% zirconia and 20% resin)				
Viscosity (cp)	15000	16000	17000	18000
Corresponding shear rate	44.37	43.54	42.71	41.89
Printing speed (mm/s)	7.35	6.94	6.53	6.11

Since the nozzle tip used in this machine is a pointed needle, excessively high printing speeds resulted in clogging of nozzle. Thus, the printing speed corresponding to the viscosities of 15000 and 16000 cp were found to be inappropriate. Furthermore, the lower viscosity of the slurry also compromises the structural stability and integrity of the printed parts. Based on the experimental analysis, a printing speed of 6.53 mm/s was found to be the optimal speed at which ceramic printing can be carried out without any clogging issues.

3.1.4 Printing angle

This study utilizes PETG as a support material which provides stability to the printed ceramic slurry. The more contact surface between the ceramic material and the support material, the higher the success rate of printing. However, this stability comes at the expense of the rough surface of the final printed part. Thus, it becomes necessary to minimize the support and use it only at extremely intricate locations. To benchmark, this study prints a pyramid with an angle of 45˚

between the wall and base as shown in Figure 3. During the subsequent printing tests, the subtended angle in the design is increased by 5˚and checked for support requirements. The printed pyramid designs at different subtended angles are shown in Figure 5. As can be seen in Figure 5a, the pyramid with the subtended angle of 45˚ is distorted with excessive sagging. Thus, such designs require PETG support to withhold the integrity of the design. Furthermore, as illustrated in Figure 5b the pyramid design with the subtended angle of 50° maintains the geometric shape without the requirement of support. However, it can be observed that but it can be observed that the ceramic slurry has a tendency to flow downward, causing slight sagging. The pyramid structures with subtended angles of 55° and 60° as depicted in Figures 5c and 5d, respectively can maintain the geometric shape without any support requirements. Thus, this study concludes that the PETG support is necessary for the designs that include subtended angles of ≤ 50˚.

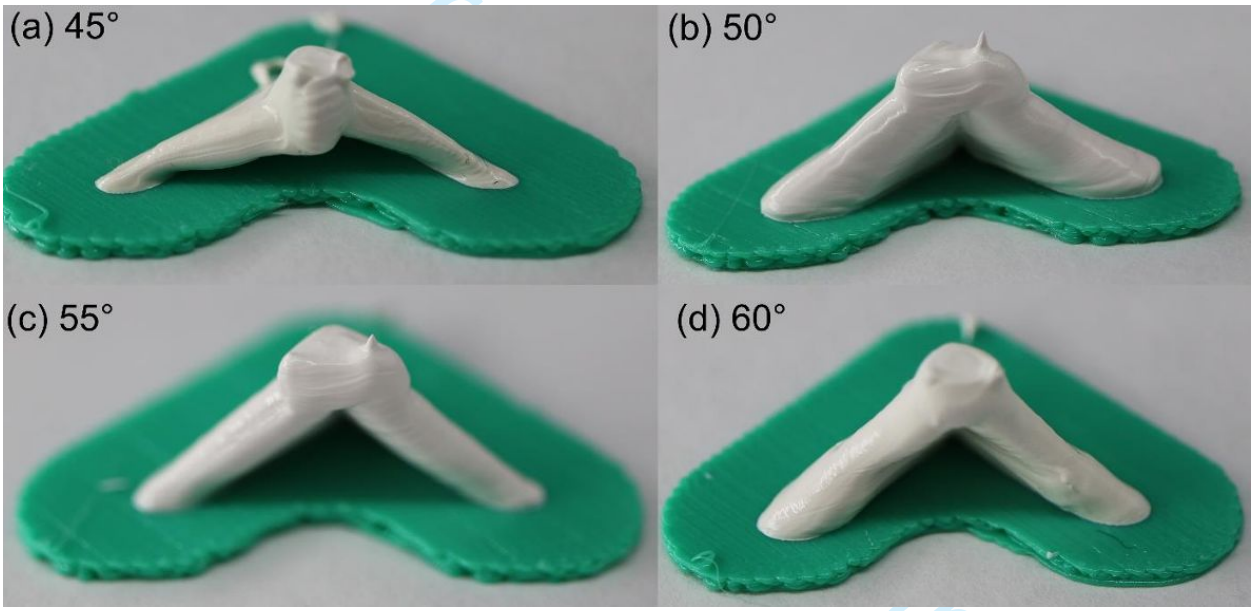

Figure 5: Evaluation of support requirement for the pyramid designs with the subtended angles of (a) 45^0, (b) 50^0, (c) 55^0, and (d) 60^0.

3.2 Thermogravimetric (TGA) and Differential Scanning Calorimetry (DSC) Analysis of Two Different Compositions of Zirconia Slurry

The thermogravimetric analysis results are illustrated in Figure 6. The 70/30 and 80/20 compositions indicate that the weight of both ceramic slurries slightly decreases at 100°C. This

decrease in weight is attributed to the elimination of moisture that the green body contains. To ensure complete removal of moisture content a constant temperature of 100°C is maintained for 1 hour. The resin in both compositions begins to evaporate at 380°C which is represented by the abrupt drop in weight in Figure 6. The green body is held at this temperature for 2 hours to ensure uniform heating throughout the objects. Subsequently, the temperature is gradually increased to 600°C to ensure the completion of debinding process.

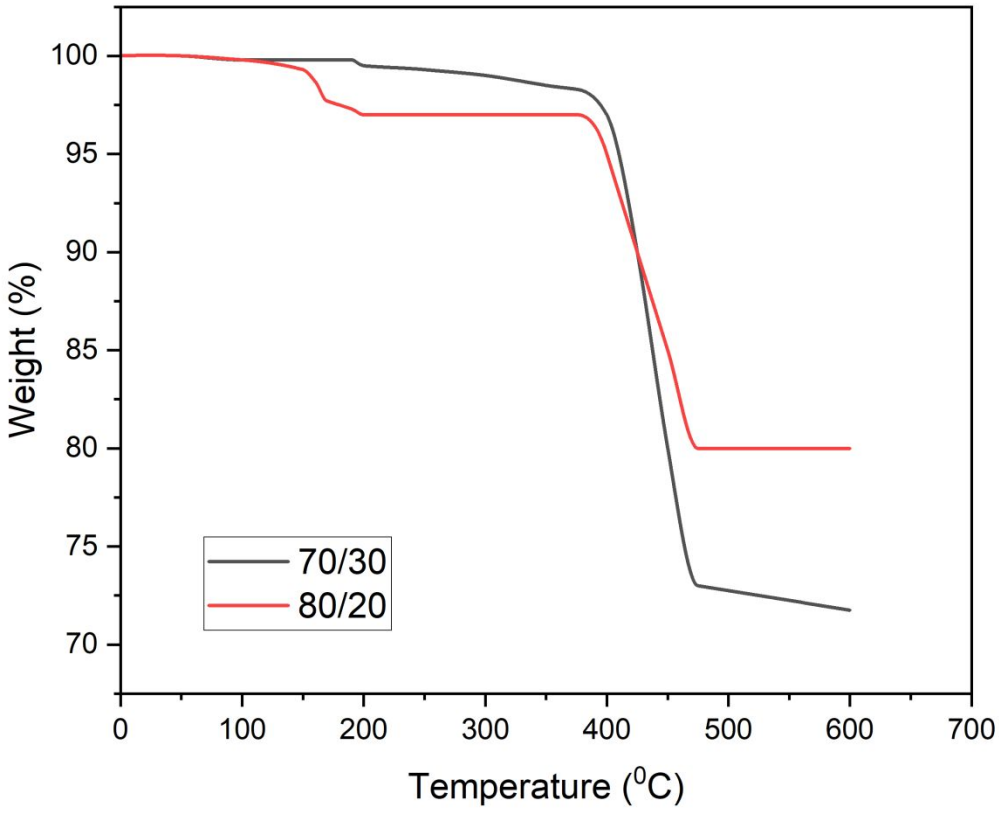

Figure 6: TGA results of two different compositions of zirconia slurry showing thermal degradation and evaporation of binder starting at 380ºC.

Figure 7 shows the two-phase sintering employed in this study. The temperature of the green body is gradually increased to 800˚C which results in complete debinding (i.e. evaporation of resin and moisture). The temperature is increased from 800 ˚C to 1550˚C at a constant rate during which zirconia undergoes a phase change to a tetragonal crystal phase from a monoclinic crystal (Song, Ding et al. 2023). Maintaining the temperature at 1550°C for a prolonged time will stabilize this

ceramic crystal phase change. Once the complete phase transformation is ensured, the sintered part is cooled to the room temperature as shown in Figure 7.

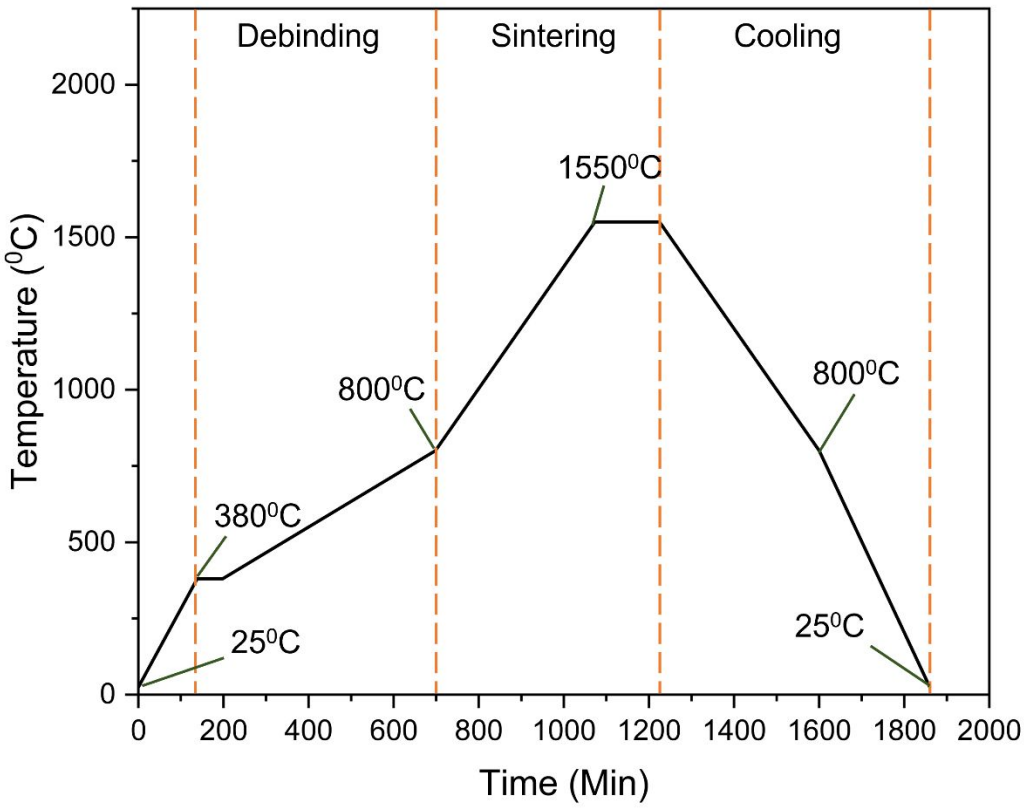

Figure 7: Two-phase sintering and their corresponding temperature of zirconia green body.

The DSC (differential scanning calorimetry) analysis was performed to investigate the thermal behavior of the two resin compositions (70/30 and 80/20) during the heating process. Figure 8 presents the corresponding DSC curves. The DSC curves for both compositions exhibit significant differences, reflecting the impact of zirconia content and the resin mixture on thermal properties. For the 70/30 composition, a distinct endothermic peak is observed at approximately 400°C, followed by a sharp exothermic peak around 500°C. This behavior corresponds to the decomposition and volatilization of organic components, particularly TMPTA, which is present in significant amounts in this composition.

In contrast, the 80/20 composition shows a less intense endothermic peak compared to the 70/30 composition. The absence of TMPTA in the 80/20 composition contributes to the observed differences. The increased zirconia content (80 wt.%) and higher HDDA percentage enhance thermal stability, reducing the intensity of the thermal transitions. Additionally, the 80/20

composition demonstrates a smaller exothermic peak, indicating that the resin is largely cured before the thermal decomposition process begins. The endothermic events below 200°C in both compositions correspond to the evaporation of residual cleaning agent (alcohol) and moisture in the samples. The onset of decomposition for organic materials is slightly delayed in the 80/20 composition due to its higher zirconia loading, which likely inhibits the thermal transfer to the resin matrix. The results confirm that the choice of resin components and zirconia content significantly impacts the thermal behavior. The higher solid loading in the 80/20 composition ensures better thermal stability, which is critical for achieving dimensional accuracy during the sintering process.

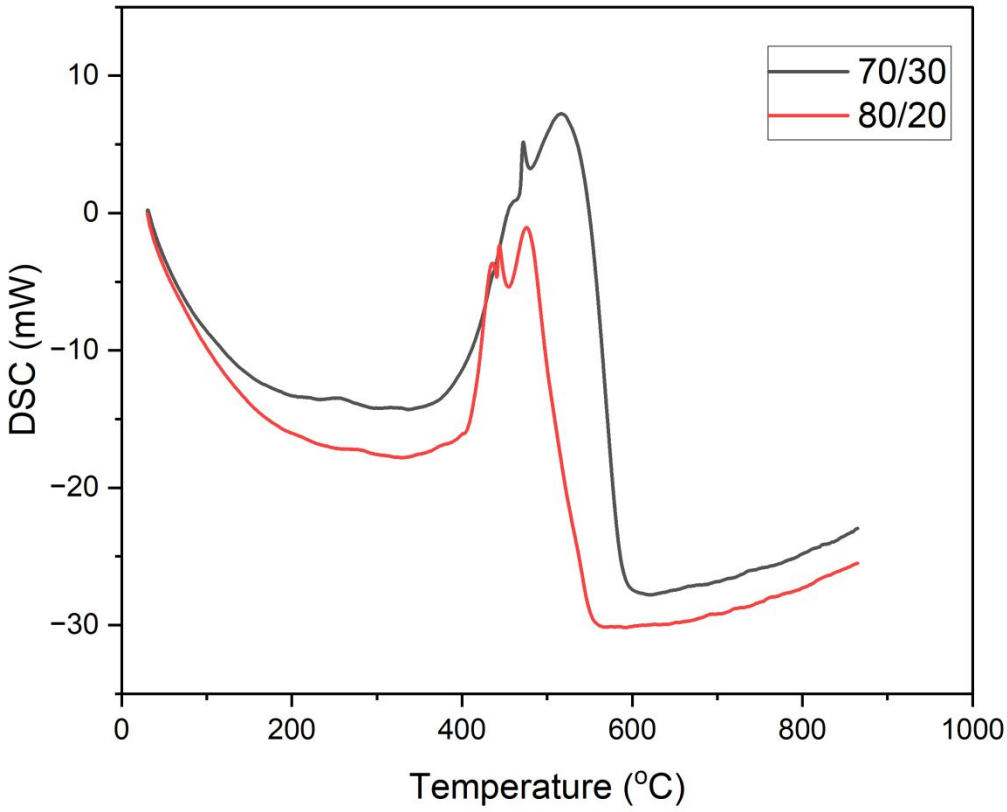

Figure 8: DSC analysis of two compositions (zirconia/resin = 70/30 and 80/20).

3.3 Shrinkage Analysis

This study determines the volumetric reduction of the printed part after sintering. To evaluate the percentage of shrinkage, the dimensions of the sample before and after sintering were calculated. Table 6 shows the linear and volumetric shrinkage rates that were examined for zirconia slurry with a 70/30 composition. The average linear shrinkage was 29.37%, and the average

volumetric shrinkage was 64.78%. For zirconia slurry with 80/20 composition, the average linear shrinkage was 26.24%, and the average volumetric shrinkage was 59.88% (Table 6).

The theoretical volumetric shrinkage for the 70/30 and 80/20 compositions of zirconia slurry is calculated to be 70.33% and 59.72%, respectively. The experimental results found that the actual shrinkage rate for the 80/20 weight zirconia slurry was consistent with the theoretical volumetric shrinkage rate (Elsen and Ramesh 2016, Romario, Bhat et al. 2024). This shrinkage was also validated using the SEM analysis depicted in Figure 9.

For the 70/30 zirconia slurry composition, a difference of 5.55% was observed between the theoretical and actual volumetric shrinkages. This difference is predicted to be due to the lower powder composition, which tends to generate porosity during the sintering process (Mazlan, Jamadon et al. 2023). As a result, the sintered object contains internal voids, which contributes to the discrepancy in shrinkage rates.

Table 6: Shrinkage analysis of the samples fabricated with zirconia slurry.

Composition	Axis	Green Body (mm)	Sintered Part (mm)	Linear Shrinkage (%)	Volume Shrinkage (%)
70/30	X	10.05	7.15	28.85	64.78
	Y	10.05	7.12	29.15	
	Z	9.99	6.98	30.13	
80/20	X	9.95	7.44	25.23	59.88
	Y	10.1	7.48	26.23	
	Z	9.94	7.23	27.26	

Figures 9a and 9b show the average layer thickness post-sintering for the 80/20 and 70/30 weight compositions which are evaluated to be 144 µm and 138 µm, respectively. Given that the layer thickness used in this fabrication was 0.2 mm, this shrinkage corresponds to the linear shrinkage in the Z-axis. Thus, the linear shrinkage rate is consistent with the experimental results.

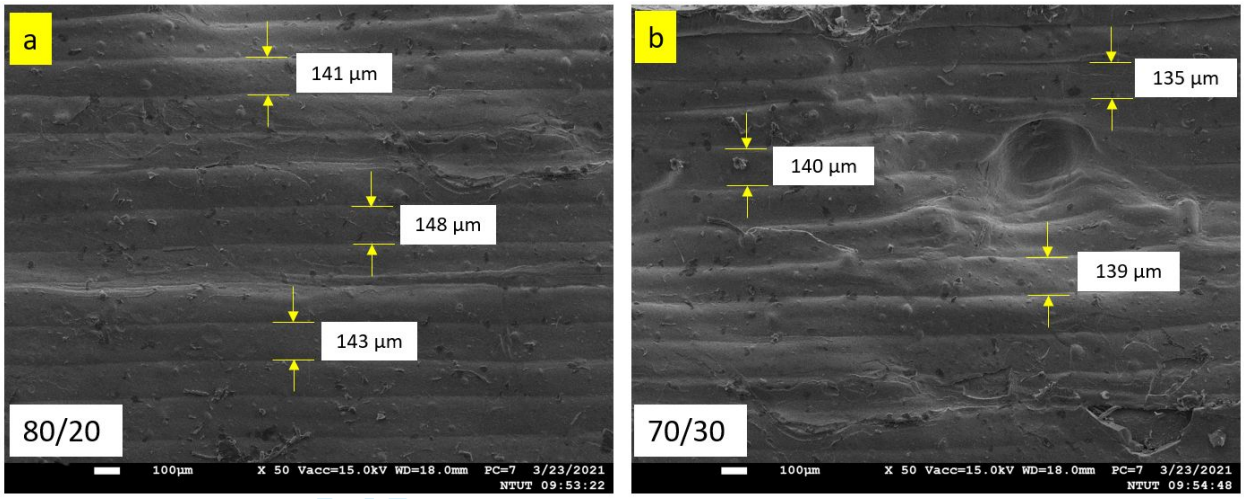

Figure 9: SEM of the layer thickness of zirconia sintered part: a) 80/20 composition and b) 70/30 composition.

Figure 10a illustrates the SEM micrograph of the sintered ceramic sample, revealing a dense microstructure with evidence of porosity. The pores depicted by the arrows are formed due to the gas venting during the debinding process. These pores are a result of the volatilization of resin components as they are thermally decomposed and evaporated. While the majority of the material appears well-sintered, the presence of large-scale porosity could affect the final mechanical properties, including strength and density. Figure 10b presents the particle size distribution of the zirconia powder used in the study. The data indicates a mean particle diameter of approximately 0.719 µm, with the majority of particles ranging below 3 µm. The narrow particle size distribution as shown in Figure 10b contributes to better packing density during the green body fabrication process, which is essential for uniform sintering. Smaller particle sizes enhance sinterability by increasing the surface area for atomic diffusion, leading to improved densification. However, excessively small particles may exacerbate issues like agglomeration and porosity due to incomplete packing or gas entrapment during processing (Bai, Wagner et al. 2017).

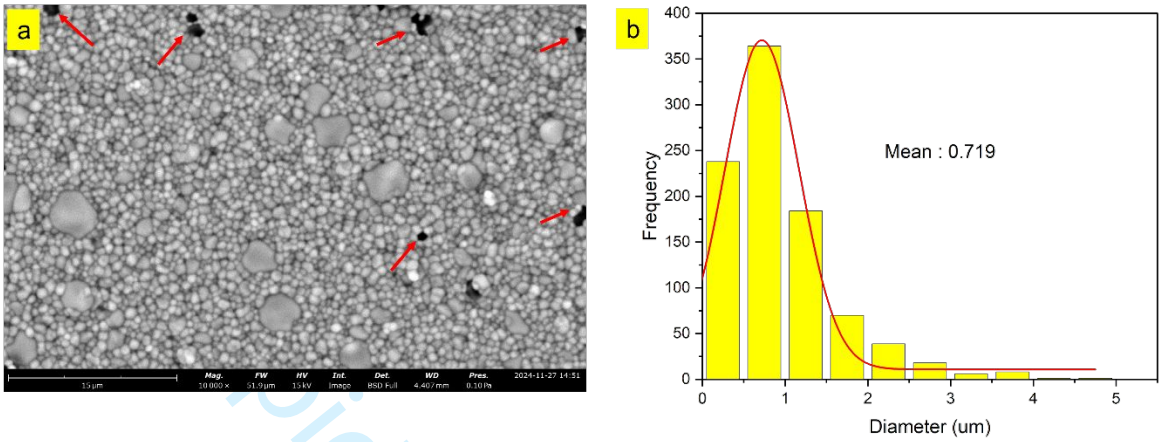

Figure 10: Micrograph of 3D printed zirconia (sintered): (a) morphology of sintered part (b) particle size distribution analysis.

3.4 Energy Dispersive Spectroscopy (EDS) Analysis

Figure 11 shows the EDS analysis of the sintered ceramic sample. As can be seen, the sintered ceramic predominantly consists of zirconium (Zr) and oxygen (O) at 70.43% and 25.28%, respectively. This indicates a successful fabrication of the zirconia (ZrO_2) matrix, with oxygen molecules aligning well with the stoichiometry of zirconia. The presence of yttrium (Y) at 3.59% suggests the incorporation of yttria (Y_2O_3) as a stabilizer, enhancing fracture toughness and stabilizing the tetragonal phase, which improves mechanical properties and resistance to thermal cycling.

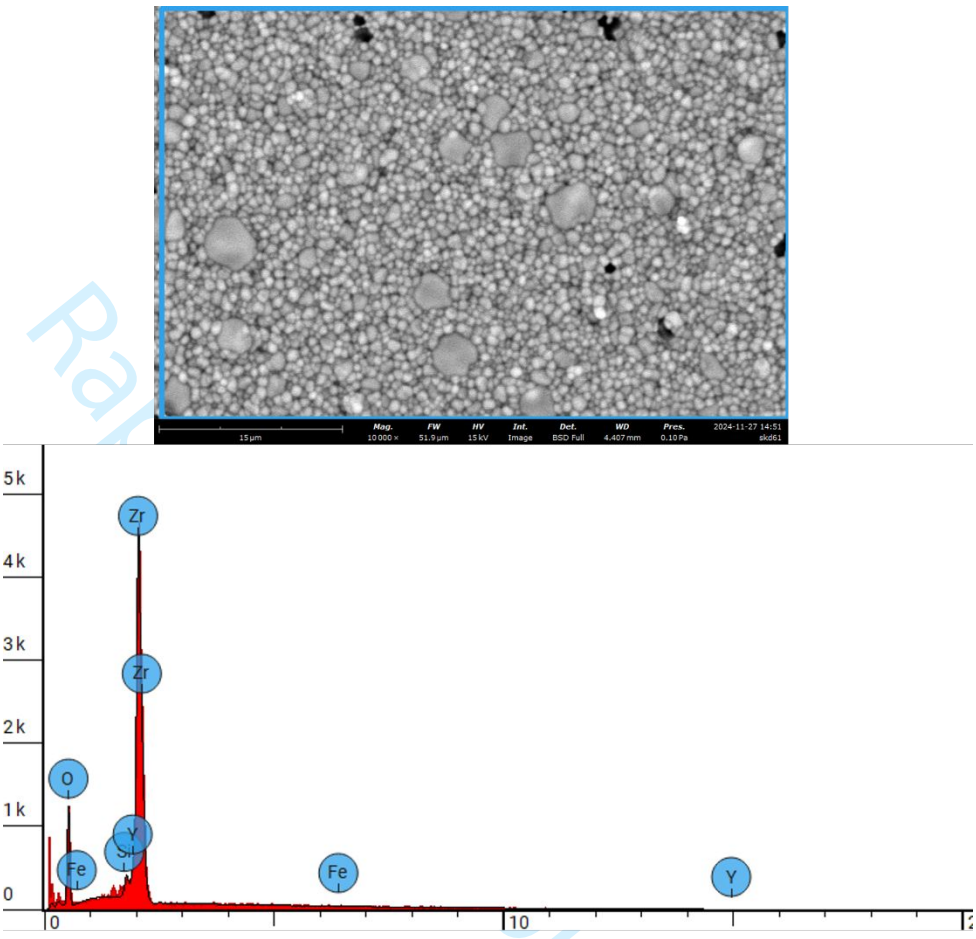

Weight %

	O	Si	Fe	Y	Zr
Zr - sintered	25.28	0.30	0.40	3.59	70.43

Figure 11: EDS analysis of 3D printed part (zirconia sintered).

3.5 X-Ray Diffraction (XRD) Analysis

The XRD pattern of the sintered zirconia (ZrO_2) sample, printed using the self-developed 3D printing system is shown in Figure 12. The major peaks observed at 2θ angles at 30.99°, 50.93°, and 60.00° correspond to the planes (101), (112), and (211), respectively, confirming the presence of the tetragonal phase of zirconia, which is stabilized by yttria (Y_2O_3) as seen in the EDS results. The absence of significant peaks associated with monoclinic or cubic phases further validates the success of the fabrication process in producing predominantly tetragonal zirconia.

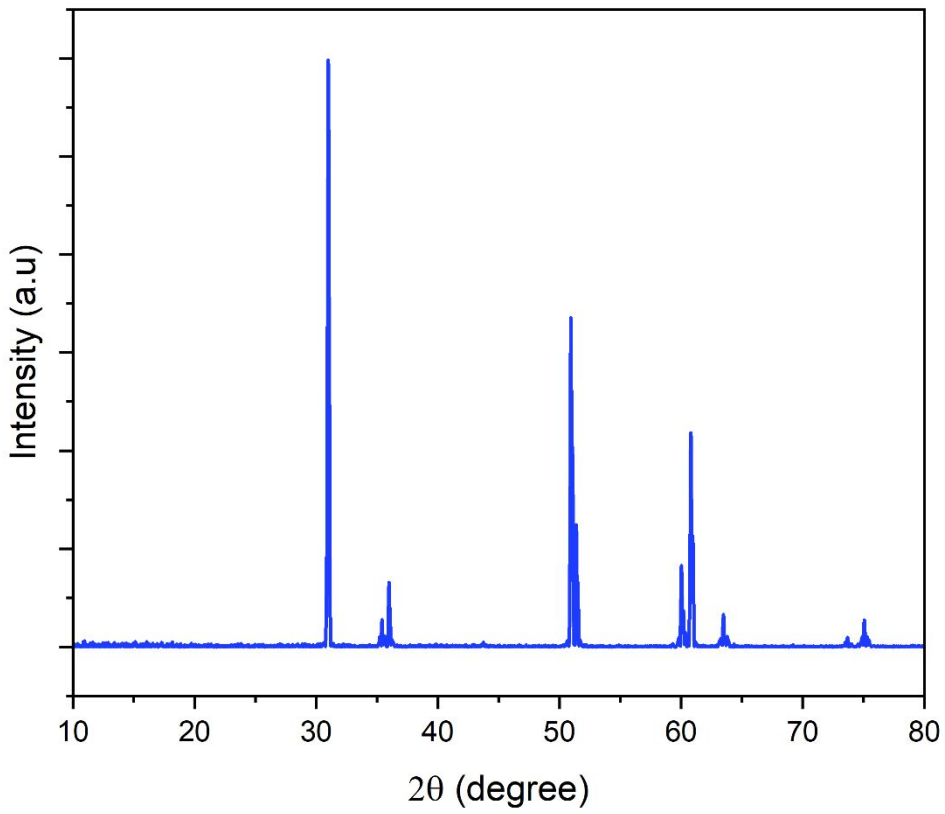

Figure 12: XRD analysis of 3D printed part (zirconia sintered).

3.6 Extrusion Infill Density Vs. Shrinkage

The extrusion of the material can be adjusted to control the internal filling, thereby reducing the ceramic slurry. This study was conducted to evaluate the effect of controlled infill density on the shrinkage of the samples upon sintering. To determine whether different infill levels affect the shrinkage rate, tests were conducted with the 70/30 composition at 40%, 60%, 80%, and 100% infill levels. Figure 13 shows the post-sintering dimensional changes of the samples with different infill levels.

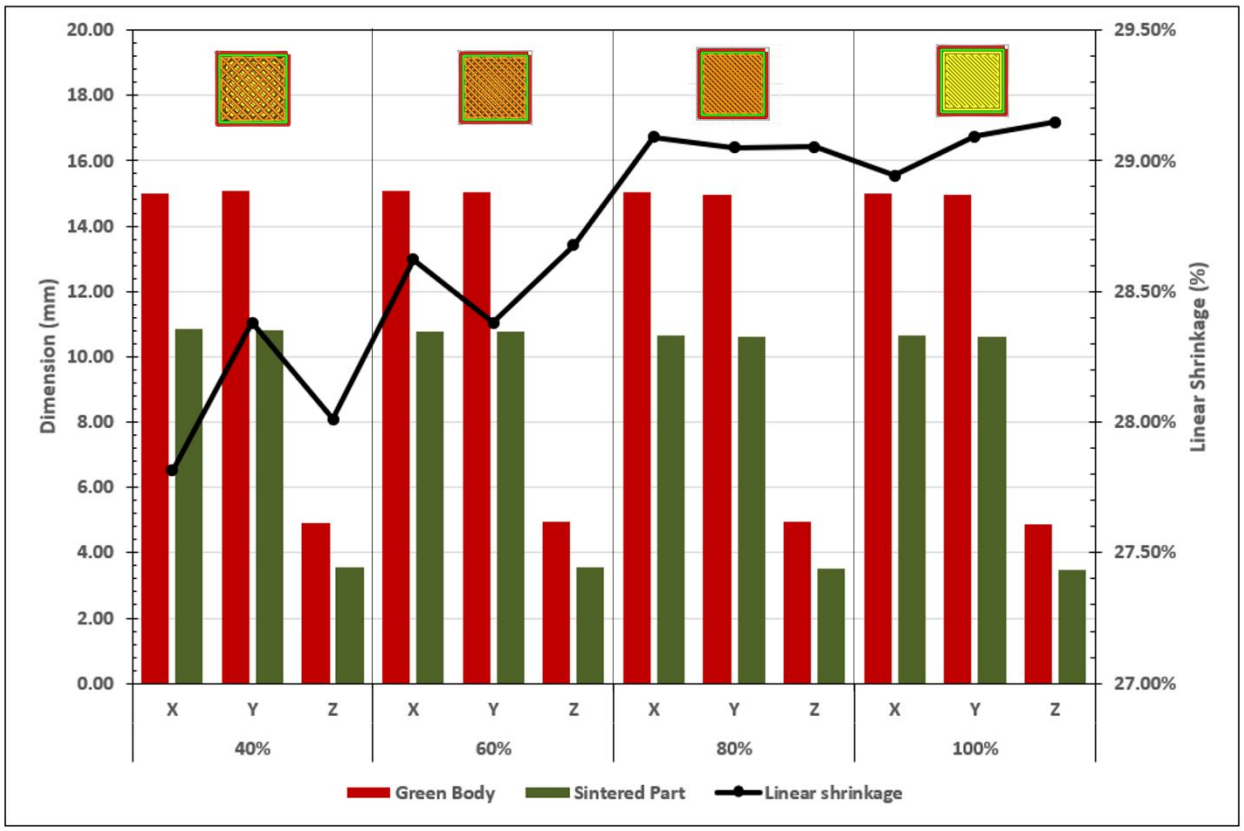

Figure 13: Effect of different infill levels on the shrinkage of the samples post-sintering.

As can be seen in Figure 13, the average shrinkage rate for the 40% infill is observed to be 28.07%. Furthermore, a 40% infill requires at least five top layers to ensure successful closure, as the default three layers generally result in fabrication failure. The shrinkage rates for 60%, 80%, and 100% infill are 28.54%, 29.07%, and 29.06%, respectively. It can be observed that the shrinkage rates for 80% and 100% infill closely match the volumetric shrinkage rate as explained in the previous section (section 3.3). Table 7 shows the effect of extrusion infill density on the linear and volumetric shrinkages. The results indicate that an infill level of 80% or higher can achieve a shrinkage rate close to that of a 100% infill.

Table 7: Effect of extrusion infill density on the linear and volumetric shrinkages.

Extrusion infill density	Shrinkage (%)			
	X – axis	Y – axis	Z – axis	Volumetric
40%	27.82	28.38	28.00	62.77
60%	28.60	28.38	28.65	63.51

80%	29.10	29.04	29.08	64.31
100%	28.92	29.10	29.15	64.29

3.7 Mechanical Properties Evaluation

The hardness and flexural strength of the fabricated samples were examined for both compositions: 70/30 and 80/20. Figure 14 shows the average hardness and flexural strength of the zirconia samples at two different compositions. It can be observed from Figure 14 that the samples with the 80/20 composition show an average hardness value of 1525 HV which is ~3% higher than that of the 70/30 composition (1480 HV). The lower hardness of the 70/30 composition is attributed to incomplete sintering shrinkage, which leaves pores within the material and results in lower hardness.

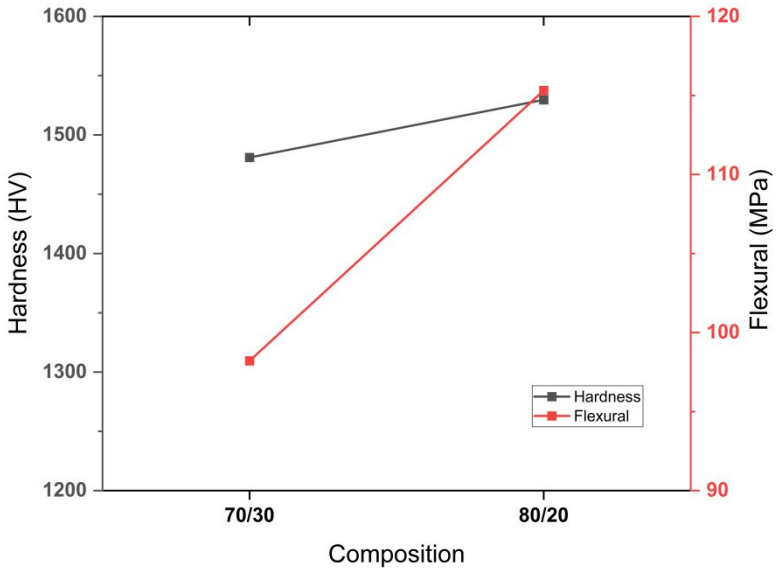

Figure 14: Hardness and flexural strength analysis of zirconia sintered part at two different compositions.

A similar observation was also obtained with the three-point bending test results which show the flexural strengths of 97 MPa and 115 MPa for the compositions 70/30 and 80/20, respectively. The results were observed to be significantly lower than that of the theoretical values. It is believed that this is due to the surface defects in the extrusion printing process, which is a known drawback

of this additive manufacturing process. These defects cause stress concentration which results in early failure of the samples. Additionally, during the printing process, deformation caused by UV light curing leads to internal cracks, making the internal structure unstable and resulting in low flexural strength. Nevertheless, owing to the vast scope of applications that can be delivered with this novel technology, there is a future scope for enhancing flexural strength by improving manufacturability.

3.8 3D Printed Prototype and Future Scope

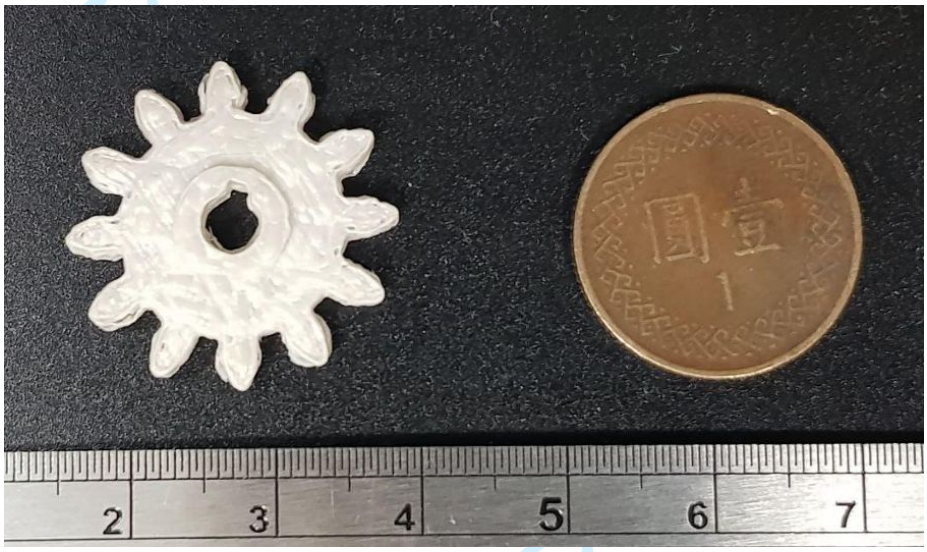

Figure 15: Demonstration of post-sintered mechanical gear prototype fabricated with zirconia slurry.

Finally, through the adjustment of various printing parameters and evaluating the shrinkage and mechanical properties, suitable printing parameters for this 3D printer were determined. The slurry composition (formula) was optimized to obtain the best outcomes in terms of its speed and precision of printing. Figure 15 shows the demonstrational prototype of the mechanical gear after sintering at a temperature of 1530°C. The overall diameter of the gear was maintained to be within 20 mm which shows the high controllability of the self-constructed 3D printer.

Though this study has solely focused on the development of a dual-nozzle slurry extrusion 3D printer, further studies are required to increase the quality and reliability of the printed parts. This study has carried out the preliminary process parameters optimization that would print the samples with acceptable accuracy and precision. Furthermore, attempts have been made to

evaluate the shrinkage and mechanical properties of the ceramic parts. The main objective of this study was to introduce the novel concept of ceramic printing using the material extrusion process and carry out preliminary evaluations. However, there is a greater scope for increasing the precision of the printer that would be able to print the intricate lattice structures with much higher accuracy. Furthermore, this 3D printer can also be used to fabricate ceramic-polymer composites that would deliver high-strength lightweight properties.

4. Conclusions

This research proposes the development of a dual-nozzle slurry extrusion 3D printer capable of achieving slurry photopolymerization. The existing multi-nozzle material extrusion 3D printing technology is modified with a specialized ceramic slurry extrusion system along with an in-built curing system. This modification can accomplish simultaneous extrusion and curing of high-viscosity slurry, thereby achieving high material utilization. Compared to the existing vat photopolymerization technology, this novel technology can fabricate ceramic components at a much higher speed and controllability without compromising the accuracy of the component. The ceramic material is used in the form of slurry mixed with a photoinitiator, which cures when exposed to UV light, allowing the printed part to maintain its shape during the printing process. Utilizing this technology with enhanced manufacturability and controllability would realize the easy fabrication of intricate ceramic lattice structures. This technology can also be utilized to fabricate ceramic-polymer composites that can deliver high mass-specific strength. Some of the important findings related to this study are listed as follows:

1. The optimal printing parameters for this machine are: a nozzle diameter of 0.6 mm and a layer thickness of 0.2 mm. The printing speed is adjusted according to the viscosity of the slurry. A slower printing speed results in more stable ceramic slurry extrusion but requires a longer time to complete the fabrication of components.
2. The overhang angle that can be printed with this system is greater than 50˚. For angles below 50˚, additional PETG support is required to maintain the shape and integrity of the object being fabricated.
3. TGA analysis reveals that the resin in both compositions begins to evaporate at 380°C which is represented by the abrupt drop in weight. The onset of debinding starts after the completion

of resin evaporation at 600°C. The DSC analysis highlights the impact of zirconia content and the resin mixture on thermal properties with 70/30 composition showing a distinct endothermic peak at approximately 400°C, followed by a sharp exothermic peak around 500°C. In contrast, the 80/20 composition shows a less intense endothermic peak ensuring better thermal stability and reducing the intensity of the thermal transitions.

4. The XRD analysis reveals major peaks at 2θ angles at 30.99°, 50.93°, and 60.00° correspond to the planes (101), (112), and (211), respectively, confirming the presence of the tetragonal phase of zirconia, which is stabilized by yttria (Y_2O_3). This is further concluded by EDS analysis.
5. The average linear and volumetric shrinkage for samples with 70% zirconia composition (70/30 composition) was 29.37% and 64.78%, respectively. Similarly, for zirconia slurry with 80/20 composition, the average linear shrinkage was 26.24%, and the average volumetric shrinkage was 59.88%.
6. Extrusion printing allows for adjusting the infill density in the slicer software to reduce the amount of material used. However, extremely low infill density results in induced porosity that may reduce the performance of the components. In the case of zirconia extrusion, an infill density of 80% or above can achieve similar strength and mechanical properties as that of a 100% infill density.
7. The samples fabricated with 80% zirconia slurry show higher mechanical properties with 1525 HV Vickers hardness and 115 MPa flexural strength which is 3% and 15.5% higher than the 70% zirconia samples, respectively. The poor mechanical properties of samples fabricated with 70% zirconia slurry were attributed to induced porosity.

Reference

Asif, M., J. H. Lee, M. J. Lin-Yip, S. Chiang, A. Levaslot, T. Giffney, M. Ramezani and K. C. Aw (2018). "A new photopolymer extrusion 5-axis 3D printer." Additive Manufacturing **23**: 355-361.

Bai, Y., G. Wagner and C. B. Williams (2017). "Effect of particle size distribution on powder packing and sintering in binder jetting additive manufacturing of metals." Journal of Manufacturing Science and Engineering **139**(8): 081019.

Cova, F., J. Hostaša, A. Piancastelli, L. Esposito, A. Paleari, A. Vedda and R. Lorenzi (2023). "Layered Y3Al5O12: Pr/Gd3 (Ga, Al) 5O12: Ce optical ceramics: Synthesis and photo-physical properties." Journal of the European Ceramic Society **43**(15): 7068-7075.

Elsen, S. R. and T. Ramesh (2016). "Shrinkage characteristics studies on conventional sintered zirconia toughened alumina using computed tomography imaging technique." International Journal of Refractory Metals and Hard Materials **54**: 383-394.
Hu, F., T. Mikolajczyk, D. Y. Pimenov and M. K. Gupta (2021). "Extrusion-based 3D printing of ceramic pastes: Mathematical modeling and in situ shaping retention approach." Materials **14**(5): 1137.
Huang, T., M. S. Mason, G. E. Hilmas and M. C. Leu (2006). "Freeze-form extrusion fabrication of ceramic parts." Virtual and Physical Prototyping **1**(2): 93-100.
Jankowska, M., A. Chachaj-Brekiesz, K. Trembecka-Wójciga, A. Jarzębska, M. Topa-Skwarczyńska, M. Pilch and J. Ortyl (2023). "Novel multi-material photo-curable resins containing high-performance photoinitiating systems and nano additives dedicated to 3D-VAT printing." Polymer Chemistry **14**(17): 2088-2106.
Jiang, C.-P., Y. S. Romario, C. Bhat, M. F. R. Hentihu, X.-C. Zeng and M. Ramezani (2023). "Design and fabrication of multi-material pneumatic soft gripper using newly developed high-speed multi-material vat photopolymerization 3D printer." The International Journal of Advanced Manufacturing Technology: 1-14.
Jiang, J., X. Xu and J. Stringer (2019). "Optimization of process planning for reducing material waste in extrusion based additive manufacturing." Robotics and Computer-Integrated Manufacturing **59**: 317-325.
Koski, C., B. Onuike, A. Bandyopadhyay and S. Bose (2018). "Starch-hydroxyapatite composite bone scaffold fabrication utilizing a slurry extrusion-based solid freeform fabricator." Additive manufacturing **24**: 47-59.
Lakhdar, Y., C. Tuck, J. Binner, A. Terry and R. Goodridge (2021). "Additive manufacturing of advanced ceramic materials." Progress in Materials Science **116**: 100736.
Lewis, J. A. (2006). "Direct ink writing of 3D functional materials." Advanced Functional Materials **16**(17): 2193-2204.
Li, W., A. Ghazanfari, D. McMillen, M. C. Leu, G. E. Hilmas and J. Watts (2018). "Characterization of zirconia specimens fabricated by ceramic on-demand extrusion." Ceramics International **44**(11): 12245-12252.
Mazlan, M. R., N. H. Jamadon, A. Rajabi, A. B. Sulong, I. F. Mohamed, F. Yusof and N. A. Jamal (2023). "Necking mechanism under various sintering process parameters–a review." journal of materials research and technology **23**: 2189-2201.
Nadkarni, S. S. and J. E. Smay (2006). "Concentrated barium titanate colloidal gels prepared by bridging flocculation for use in solid freeform fabrication." Journal of the American Ceramic Society **89**(1): 96-103.
Nyika, J., F. M. Mwema, R. Mahamood, E. T. Akinlabi and T. Jen (2022). "Advances in 3D printing materials processing-environmental impacts and alleviation measures." Advances in Materials and Processing Technologies **8**(sup3): 1275-1285.
Olhero, S., J. Mesquita-Guimarães, J. Baltazar, J. Pinho-da-Cruz and S. Gouveia (2022). "Conventional versus additive manufacturing in the structural performance of dense alumina-zirconia ceramics: 20 years of research, challenges and future perspectives." Journal of Manufacturing Processes **77**: 838-879.
Pelz, J. S., N. Ku, M. A. Meyers and L. R. Vargas-Gonzalez (2021). "Additive manufacturing of structural ceramics: a historical perspective." journal of materials research and technology **15**: 670-695.
Petit, C., L. Montanaro and P. Palmero (2018). "Functionally graded ceramics for biomedical application: Concept, manufacturing, and properties." International Journal of Applied Ceramic Technology **15**(4): 820-840.
Piconi, C., S. G. Condo and T. Kosmač (2014). "Alumina-and zirconia-based ceramics for load-bearing applications." Advanced ceramics for dentistry: 219-253.

Qian, L., L. Yang, G. Li, W. Jiang and Z. Fan (2020). "Effect of nano-TiO2 on properties of 3 mol% yttria-stabilized zirconia ceramic via layered extrusion forming." Journal of the European Ceramic Society **40**(13): 4539-4546.
Romario, Y. S., C. Bhat, M. Ramezani and C.-P. Jiang (2024). "Marine Waste Management of Oyster Shell Waste as Reinforcement for Clay Additive Manufacturing Components." International Journal of Precision Engineering and Manufacturing-Green Technology: 1-18.
Romario, Y. S., C. Bhat, M. Ramezani, T. Pasang, Z. Chen and C.-P. Jiang (2024). "Fabrication of translucent graded dental crown using zirconia-yttrium multi-slurry tape casting 3D printer." Journal of the Mechanical Behavior of Biomedical Materials: 106406.
Sangroniz Agudo, L., M. Fernández San Martín and P. A. Santamaría Ibarburu (2023). "Polymers and rheology: A tale of give and take."
Shao, H., D. Zhao, T. Lin, J. He and J. Wu (2017). "3D gel-printing of zirconia ceramic parts." Ceramics International **43**(16): 13938-13942.
Song, X., Y. Ding, J. Zhang, C. Jiang, Z. Liu, C. Lin, W. Zheng and Y. Zeng (2023). "Thermophysical and mechanical properties of cubic, tetragonal and monoclinic ZrO2." Journal of Materials Research and Technology **23**: 648-655.
Tang, H.-H., M.-L. Chiu and H.-C. Yen (2011). "Slurry-based selective laser sintering of polymer-coated ceramic powders to fabricate high strength alumina parts." Journal of the European Ceramic Society **31**(8): 1383-1388.
Tang, S., L. Yang, G. Li, X. Liu and Z. Fan (2019). "3D printing of highly-loaded slurries via layered extrusion forming: Parameters optimization and control." Additive Manufacturing **28**: 546-553.
Tang, S., L. Yang, G. Li, X. Liu and Z. Fan (2019). 3D printing of highly-loaded slurries via layered extrusion forming: parameters optimization and control. Addit Manuf 28 (February): 546–553.
Wang, Z., L. Wang, F. Tang and J. Chen (2024). "Multi-material additive manufacturing via fused deposition modeling 3D printing: A systematic review on the material feeding mechanism." Proceedings of the Institution of Mechanical Engineers, Part E: Journal of Process Mechanical Engineering: 09544089231223316.
Yen, H.-C. and H.-H. Tang (2008). "Developing a paving system for fabricating ultra-thin layers in ceramic laser rapid prototyping." The International Journal of Advanced Manufacturing Technology **36**: 280-287.
Yu, T., Z. Zhang, Q. Liu, R. Kuliiev, N. Orlovskaya and D. Wu (2020). "Extrusion-based additive manufacturing of yttria-partially-stabilized zirconia ceramics." Ceramics International **46**(4): 5020-5027.
Zhang, Z., T. Lin, H. Shao, Y. Zhang, L. Wang and X. Deng (2020). "Preparation of 3DGP dense zirconia parts by two-step method: staggered stacking method and printing wire deformation." Ceramics International **46**(5): 6491-6496.

thermoscientific

3

User name: Phenom-Workstation\Phenom
Contains 1 image(s) with a total of 1 analyses

01. Image 1

1 analyses: 1x region

Image 1

thermoscientific

1. Region

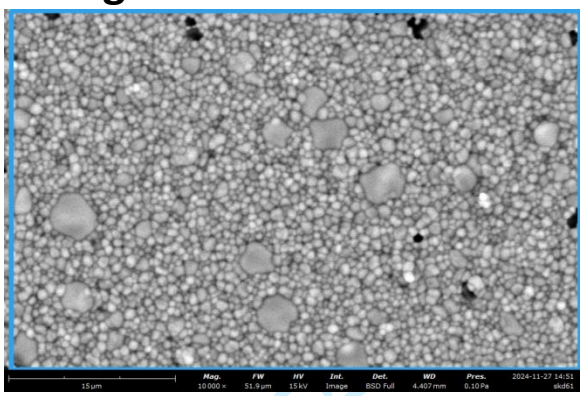

FW: 52 µm, Mode: 15 kV - Image, Detector: BSD Full, Time: 11/27/24 2:51 PM

	Element Number	Element Symbol	Element Name	Atomic Conc.	Weight Conc.	Oxide Symbol	Stoich. Weight Conc.
	8	O	Oxygen	65.546	25.275		
	14	Si	Silicon	0.443	0.300		
	26	Fe	Iron	0.297	0.400		
	39	Y	Yttrium	1.679	3.596		
	40	Zr	Zirconium	32.036	70.430		

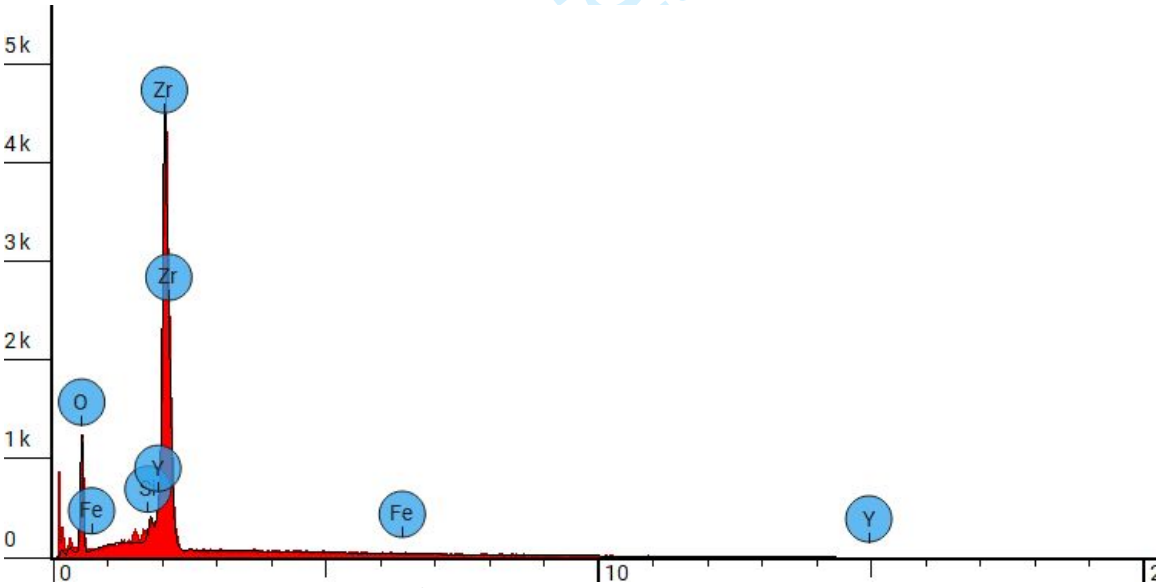

148 026 counts in 0:01:00 (2 459 c/s)

Disabled elements: Na